

Implicit to Explicit algorithm for ABAQUS Standard using User-Subroutine UMAT for a 3D Hashin Based Orthotropic Damage Model

M.R.T. Arruda^a, M. Trombini^b, A. Pagani^c

^aResearch Associate, CERIS, Instituto Superior Técnico, Universidade de Lisboa, Portugal.
(mario.rui.arruda@tecnico.ulisboa.pt)

^bPhd Student, POLITO MUL2, Politecnico di Torino, Italy.
(mattia.trombini@polito.it)

^cAssociate Professor POLITO MUL2, Politecnico di Torino, Italy.
(alfonso.pagani@polito.it)

Abstract: This paper presents research that studies a new algorithm to ease convergence of future user-subroutines UMAT, when secant material matrix is used instead of the classical tangent material matrix (aka Jacobian). This algorithm takes advantage of viscous regularization used to stabilize the numerical solution of material models with softening. This type of viscous regularization is then adapted to an UMAT, using only the secant matrix in the Newton-Raphson algorithm predictor-corrector of ABAQUS. This type of regularization may be unfit for predictor-corrector with the secant matrix, due to its implicit convergence being flawed, when the time step is smaller than the viscosity parameter, switching the algorithm into an undesired explicit form that may present convergence issues.

For this work, a new 3D orthotropic damage model with residual stresses is proposed and studied with the new algorithm, in which its convergence is tested, with classical implicit secant matrix, explicit secant matrix and the proposed implicit-to-explicit secant matrix. Also all numerical models are compared with experimental data.

Keywords: User Subroutine UMAT, Implicit to Explicit, Orthotropic Damage, 3D Hashin Failure, Composite GFRP.

1 Introduction

The necessity of researching new 3D orthotropic damage models, is mainly due to its mandatory use when simulating 3D connections in composite structures [1,2,3]. In some cases, several 2D orthotropic damage models, have been used in conjunction with shell-elements, to simulate the behaviour of exterior profiles in hybrid beams and new carbon reinforced fiber aluminium laminates [4,5]. But other authors found limitations on using classical 2D formulation with continuum shell-elements to numerically simulate 3D GFRP connections [6], related to accuracy in simulating either pilling, shear-out or bearing due to the incorrect stress distribution in the thickness in shell formulation for non-linear analysis. Due to the rapid proliferation of composite structures in the engineering industry [7], the need of a more wide 3D orthotropic damage formulation is being pursued since the beginning of 2000s [8] for structural design. The accuracy of the computed stress level depends on the problem being analysed at the micro, meso or

macro scale [9], in which in all cases must always be formulated in 3D. The application of a full 3D orthotropic damage model still presents some challenges for the structural designer such as: full 3D formulation with explicit material parameters; simple and clear guidelines for direct application. These two aspects are fundamental for the structural designer, since in the scientific community, these damage orthotropic damage models are basically used to validated experimental campaign and adopted material properties [10]. Unfortunately the use of composite orthotropic damage models by academic researchers, are not being used without an existing experimental campaign to achieve better design solutions, and this is an engineering fundamental need in the industry of composites due to the lack of structural codes for these materials.

1.1 Objectives

This work is divided in two fundamental objectives. The first is to study the numerical efficiency of a new 3D orthotropic damage model based in Hashin failure criterion, using classical MTL damage progression [11] with energy regularization [12]. This orthotropic damage model is compared and validated with experimental data. The second study consists in investigating the new algorithm ITE-UMAT to ease the convergence of the UMAT subroutine when the secant matrix is used in the predictor-corrector instead of the classical tangent matrix. The algorithm is compared with a fully implicit and explicit numerical results.

1.2 Research Significance

According to the author's best knowledge, the use of 3D orthotropic damage model with residual stresses using viscous regularization and the secant matrix for the predictor-correct algorithm has not been fully studied and validated. This work plans to fill this gap in knowledge.

2 Recent Advances in 3D Orthotropic Damage Models

Since 2000s, several 3D orthotropic damage models have been proposed, this is mainly due to the popularity in the scientific community of commercial finite element software in implementing new material constitutive relations [13,14].

Before the mass proliferation of 3D orthotropic damage models, simple 2D orthotropic damage models were used for shell elements, due to the composite ply-by-ply behaviour and simplification in the formulation [15]. These 2D orthotropic damage models were sufficient to simulate beams [5], columns [16] and composite sandwich panels [17], but with severe limitations when simulating of 3D beam-to-column connections [6].

The difficulty in evolving from a 2D to a 3D failure model, is mainly to the first being assembled and tested using plane analysis [18], this leads to different results when a formulation is then extended in the 3rd dimension [19]. In addition, the 3D failure criterion and damage evolution may depend severely on the type of orthotropic composite material being studied. The use of 3D Hashin failure criterion is not new and has been proposed for shell elements [20] and for solid elements [21,22], in any case without any proposal for the interlaminar failure. A popular 3D method based on the combination of several elliptic surfaces for the adoption of separated failure criteria [23], presenting encouraging results in simulating connection of 3 bolt joints for T300/5228A composite material, with discontinuous damage evolution. Some variations of these elliptic surfaces were used for stochastic analysis of peek laminates [24]. For composite fibre metals, fibre and matrix 3D failure criteria are based on a square root sum of total strains [25], but with a cohesive interlaminar failure criterion. A variation of this last method was applied in FRP

composites [26,27], but with limitations to material orientation on the failure criterion. One of the first successful applications in 3D analysis with Larc05 was presented in the work of [28], with variation proposed by [29]. 3D failure criteria with simple degradation models [30] in terms of elastic parameters have also been successful, and continue to be popular among structural engineers, due to its simplicity of implementation. One of the most successful applications of a fully 3D Hashin failure criterion with simple degradation models was proposed by [31], for bolted connections. Recently the Hou criteria, based on an enhanced 3D elliptic failure surface [32], using explicit formulation to simulate drilling damage. To improve the matrix damage evolution due to higher shear, the NU failure criterion was proposed and applied in three-point bending load [33]. Recently the use of invariant base formulation started to produce great results, concerning the bearing in composite connections [34,35].

3 3D Orthotropic Stiffness Formulation

To ease the orthotropic formulation description in the UMAT subroutine, ABAQUS standard notation is used for both stress and strain tensors [36]. The elastic constitutive relation for the stress and strain are based on the compliance and stiffness matrix respectively (1).

$$\varepsilon_i = H_{ij}\sigma_j \quad [H_d]^{-1} = [C_d] \quad \sigma_i = C_{ij}\varepsilon_j \quad (1)$$

with:

$$\begin{aligned} \sigma_1 &= \sigma_{11}; \sigma_2 = \sigma_{22}; \sigma_3 = \sigma_{33}; \sigma_4 = \tau_{12}; \sigma_5 = \tau_{13}; \sigma_6 = \tau_{23} \\ \varepsilon_1 &= \varepsilon_{11}; \varepsilon_2 = \varepsilon_{22}; \varepsilon_3 = \varepsilon_{33}; \varepsilon_4 = \gamma_{12}; \varepsilon_5 = \gamma_{13}; \varepsilon_6 = \gamma_{23} \end{aligned} \quad (2)$$

To present a coherent and thermodynamic admissible 3D orthotropic stiffness, it's necessary to assemble the damage compliance matrix H_d , using exclusively the diagonal term to take into account the damage behaviour [37,29] (8). It is then possible to assemble the damaged stiffness matrix C_d , by inverting the previous compliance matrix (10). It is important to state the relevance of Γ_d , since this term guarantees that when subjected to uniform longitudinal stress, no transversal stress occurs. Just like in the previous 2D Hashin formulation [15], the tension and compression damage (d_t, d_c) is activated using the respective effective stress space (3). For this work damage variables are related to the fibre d_f , the matrix d_m and the interlaminar d_i .

$$\hat{\sigma}_i = \frac{\sigma_i}{(1 - d_i)} \quad (3)$$

where:

$$d_1 = d_f; d_2 = d_m; d_3 = d_i; d_4 = d_{s12}; d_5 = d_{s13}; d_6 = d_{s23}$$

with:

$$d_f = \begin{cases} d_{ft} & \text{if } \hat{\sigma}_1 \geq 0 \\ d_{fc} & \text{if } \hat{\sigma}_1 < 0 \end{cases} \quad (4)$$

$$d_m = \begin{cases} d_{mt} & \text{if } \hat{\sigma}_2 + \hat{\sigma}_3 \geq 0 \\ d_{mc} & \text{if } \hat{\sigma}_2 + \hat{\sigma}_3 < 0 \end{cases} \quad (5)$$

$$d_i = \begin{cases} d_{it} & \text{if } \hat{\sigma}_3 \geq 0 \\ d_{ic} & \text{if } \hat{\sigma}_3 < 0 \end{cases} \quad (6)$$

$$\begin{cases} d_{s12} = 1 - (1 - d_{ft})(1 - d_{fc})(1 - d_{mt})(1 - d_{mc}) \\ d_{s13} = 1 - (1 - d_{ft})(1 - d_{fc})(1 - d_{it})(1 - d_{ic}) \\ d_{s23} = 1 - (1 - d_{mt})(1 - d_{mc})(1 - d_{it})(1 - d_{ic}) \end{cases} \quad (7)$$

The main advantage is that this matrix by design verifies the thermodynamic admissibility principals, when using the Gibbs free energy (14) [38,39].

$$[H_d] = \begin{bmatrix} \frac{H_{11}}{1 - d_f} & H_{12} & H_{13} & 0 & 0 & 0 \\ H_{21} & \frac{H_{22}}{1 - d_m} & H_{23} & 0 & 0 & 0 \\ H_{31} & H_{32} & \frac{H_{33}}{1 - d_i} & 0 & 0 & 0 \\ 0 & 0 & 0 & \frac{H_{44}}{1 - d_{s12}} & 0 & 0 \\ 0 & 0 & 0 & 0 & \frac{H_{55}}{1 - d_{s13}} & 0 \\ 0 & 0 & 0 & 0 & 0 & \frac{H_{66}}{1 - d_{s23}} \end{bmatrix} \quad (8)$$

with:

$$\begin{cases} H_{11} = \frac{1}{E_1} \\ H_{22} = \frac{1}{E_2} \\ H_{33} = \frac{1}{E_3} \end{cases} \quad \begin{cases} H_{12} = H_{21} = -\frac{v_{12}}{E_1} \\ H_{13} = H_{31} = -\frac{v_{13}}{E_1} \\ H_{23} = H_{32} = -\frac{v_{23}}{E_2} \end{cases} \quad \begin{cases} H_{44} = G_{12} \\ H_{55} = G_{13} \\ H_{66} = G_{23} \end{cases} \quad (9)$$

$$[C_d] = \Gamma_d \begin{bmatrix} C_{11} & C_{12} & C_{13} & 0 & 0 & 0 \\ C_{21} & C_{22} & C_{23} & 0 & 0 & 0 \\ C_{31} & C_{32} & C_{33} & 0 & 0 & 0 \\ 0 & 0 & 0 & C_{44} & 0 & 0 \\ 0 & 0 & 0 & 0 & C_{55} & 0 \\ 0 & 0 & 0 & 0 & 0 & C_{66} \end{bmatrix} \quad (10)$$

with:

$$\begin{cases} C_{11} = (1 - d_f)E_1[1 - (1 - d_m)(1 - d_i)v_{23}v_{32}] \\ C_{22} = (1 - d_m)E_2[1 - (1 - d_f)(1 - d_i)v_{13}v_{31}] \\ C_{33} = (1 - d_i)E_3[1 - (1 - d_f)(1 - d_m)v_{12}v_{21}] \\ C_{12} = C_{21} = (1 - d_f)(1 - d_m)E_1[v_{21} + (1 - d_i)v_{31}v_{23}] \\ C_{13} = C_{31} = (1 - d_i)(1 - d_m)E_1[v_{31} + (1 - d_m)v_{21}v_{32}] \\ C_{23} = C_{32} = (1 - d_m)(1 - d_i)E_2[v_{32} + (1 - d_f)v_{31}v_{12}] \end{cases} \quad (11)$$

$$\begin{cases} C_{44} = (1 - d_{s12})G_{12}/\Gamma_d \\ C_{55} = (1 - d_{s13})G_{13}/\Gamma_d \\ C_{66} = (1 - d_{s23})G_{23}/\Gamma_d \end{cases} \quad (12)$$

$$\begin{cases} \Gamma_d = (1 - \Gamma_{fm}v_{12}v_{21} - \Gamma_{mi}v_{23}v_{32} - \Gamma_{fi}v_{13}v_{31} - 2 \times \Gamma_{fmi}v_{12}v_{23}v_{31})^{-1} \\ \Gamma_{fm} = (1 - d_f)(1 - d_m) \\ \Gamma_{mi} = (1 - d_m)(1 - d_i) \\ \Gamma_{fi} = (1 - d_f)(1 - d_i) \\ \Gamma_{fmi} = (1 - d_f)(1 - d_m)(1 - d_i) \end{cases} \quad (13)$$

$$\Psi(\sigma, d, z) = \frac{1}{2} \{\sigma\}^t [C_d] \{\sigma\} \quad (14)$$

with:

$$\Psi(\sigma, d, z) = \frac{1}{2} \left(\sum_{i=1}^6 \frac{H_{ii}\sigma_i^2}{1 - d_i} + \sum_{i,j=1 \wedge 2}^{3 \wedge 1} 2 \times H_{ij}\sigma_i\sigma_j \right) \quad (15)$$

where:

$$\sigma_1 = \sigma_{11}; \sigma_2 = \sigma_{22}; \sigma_3 = \sigma_{33}; \sigma_4 = \tau_{12}; \sigma_5 = \tau_{13}; \sigma_6 = \tau_{23} \\ d_1 = d_f; d_2 = d_m; d_3 = d_i; d_4 = d_{s12}; d_5 = d_{s13}; d_6 = d_{s23}$$

With this orthotropic damaged stiffness, when calculating the thermodynamic forces, these are always positive (16), therefore validating the 2nd principal of thermodynamics (17), and demonstrating the damage model is thermodynamically admissible.

$$Y_i = \frac{\partial \Psi}{\partial d_i} = \frac{1}{2} \frac{H_{ii}\sigma_i^2}{(1 - d_i)^2} \geq 0 \quad (16)$$

$$\Rightarrow \sum_i Y_i \delta d_i \geq 0 \quad (17)$$

4 Adopted 3D Hashin Based Damage Model

It is important to point out, there is no consensus in the scientific community, regarding the true formulation of 3D Hashin failure criterion. This is due to the fact that the real cross failure criterion between the intralaminar and interlaminar, is still highly debatable in the scientific community [31,24]. This uncertainty is still more pronounce, when the damage evolutions laws are studied, [40,29] and several assumptions must be admitted to fully verify the thermodynamic admissibility criteria.

Contrary to popular beliefs, Hashin failure criterion started as a 3D failure criterion to be used in shell elements, and it was later simplified for the 2D plane elements, although did not possess any interlaminar failure criterion. Also, another limitation to this failure model, is that it was assembled for unidirectional composites, but many authors still use it for general lamina composites [41,42].

4.1 Hashin 3D Failure Criterion

In this work, the Hashin 3D failure criterion is based on the merge of the formulations proposed by [21], [43] and [30]. These still admit a main plane behaviour, that is consistence with e principal resistance stress of the material [6], in which its failure criteria are assembled.

The original model itself presents some material and tensor field simplifications, since the real behaviour of composites is difficult to represent in the 3D realm. In this work to extend to a fully 3D Hashin damage model, these simplifications will also be applied and explained throughout the manuscript.

The 1st simplification is that all unidirectional fibres are transversely isotropic, in which the failure criterion consists of effective stresses (18), with the plane 2-3 rotating around axis-1 [43]. Therefore, the failure criterion is defined for fibre breaking F_f in axis-1 and matrix cracking F_m for plane 2-3, using their respective tensorial plane stresses (18). Since in this work, these failure criteria are used in damage models, all the tensors are written in terms of effective stresses.

$$\begin{aligned} F_f(\hat{\sigma}_1, \hat{\tau}_{12}, \hat{\tau}_{13}) &= 1.0 \\ F_m(\hat{\sigma}_2, \hat{\sigma}_3, \hat{\tau}_{21}, \hat{\tau}_{31}, \hat{\tau}_{23}) &= 1.0 \end{aligned} \quad (18)$$

Although the Hashin criterion is always positioned in the material principal directions, it is preferable to rewrite the failure criterion functions in terms of stress invariants using envelope quadratic equations (19), to promote a more robust failure formulation similar to Von-Mises.

$$\begin{aligned} F_f(I_1, I_4) &= A_f I_1 + B_f I_1^2 + D_f I_4 = 1.0 \\ F_m(I_2, I_3, I_4) &= A_m I_2 + B_m I_2^2 + C_m I_3 + D_m I_4 = 1.0 \end{aligned} \quad (19)$$

with

$$\begin{cases} I_1 = \hat{\sigma}_1 \\ I_2 = \hat{\sigma}_2 + \hat{\sigma}_3 \\ I_3 = \hat{\tau}_{23}^2 - \hat{\sigma}_2 \hat{\sigma}_3 \\ I_4 = \hat{\tau}_{12}^2 + \hat{\tau}_{13}^2 \end{cases} \quad (20)$$

It is possible to simplify in the case of pure shear stress ($\tau_{ij}, \tau_{jl} = 0, \sigma = 0$), for each of the respective shear directions, and compute the values of D_f and C_m and D_m (21), in which S_L and S_T are the longitudinal and shear stress respectively.

$$\begin{cases} C_m = \frac{1}{S_T^2} \\ D_f = D_m = \frac{1}{S_L^2} \end{cases} \quad (21)$$

Then 2nd simplification is that the tensile and compressive failure criteria may present different failure modes for both the fibre and the matrix, resulting in different failure surface functions.

For the 3rd simplification it concedes that for the fibre buckling in compression (22), there is no influence of the shear stresses. This last simplification in the fibre for compression in 3D models has been challenged by other authors, using the fibre kinking mode [28]. Previous studies have observed the deterioration of matrix shear modulus in fibre cycle compression [44,45], in any case with small influence and still some uncertainties, therefore this simplification is still applied in this work.

For the 3rd simplification admitted only quadratic terms in the fibre failure criterion, to preserve the ecliptic envelope surface ($A_{ft} = 0; B_{ft} = 1/X_t^2$). In any case the simplification of the compressive fibre failure criterion, removes the possibility of a fully closed surface (23). X_t and X_c are the fibre tensile and compressive strength respectively.

$$\begin{aligned} A_{ft} &= 0; B_{ft} = \frac{1}{X_t^2}; D_{ft} = D_f = \frac{1}{S_L^2} \\ A_{fc} &= 0; B_{ft} = \frac{1}{X_c^2}; D_{ft} = 0 \end{aligned} \quad (22)$$

$$\begin{aligned} F_{ft} &= \left(\frac{\hat{\sigma}_1}{X_t}\right)^2 + \frac{\hat{t}_{12}^2 + \hat{t}_{13}^2}{S_L^2} \leq 1.0 & \text{if } \hat{\sigma}_1 \geq 0 \\ F_{fc} &= \left(\frac{\hat{\sigma}_1}{X_c}\right)^2 \leq 1.0 & \text{if } \hat{\sigma}_1 < 0 \end{aligned} \quad (23)$$

The 4th simplification, is acknowledging that the tensile matrix failure criterion, only depends on quadratic terms (19), which is according to some cohesive models [46], and promoting a closed failure surface function (24), (25). Y_t and Y_c are the matrix tensile and compressive strength respectively.

$$A_{mt} = 0; B_{mt} = \frac{1}{Y_t^2}; C_{mt} = \frac{1}{S_T^2}; D_{mt} = D_m = \frac{1}{S_L^2} \quad (24)$$

$$F_{mt} = \left(\frac{\hat{\sigma}_2 + \hat{\sigma}_3}{Y_t}\right)^2 + \frac{\hat{t}_{23}^2 - \hat{\sigma}_2 \hat{\sigma}_3}{S_T^2} + \frac{\hat{t}_{21}^2 + \hat{t}_{31}^2}{S_L^2} \leq 1.0 \quad \text{if } \hat{\sigma}_2 + \hat{\sigma}_3 \geq 0 \quad (25)$$

The 5th simplification is linked to the resistance of the matrix during compression, in which the collapse during biaxial behaviour is linked to crushing when $\sigma_2 = \sigma_3 = -\sigma \gg Y_c$. But it must verify the collapse during uniform compression when $\sigma_2 = -Y_c$, resulting in the following system of equations (26), when the shear stress components is 0 and we are on the onset of matrix compression failure.

$$\begin{cases} A_{mc}(\hat{\sigma}_2 + \hat{\sigma}_3) + B_{mc}(\hat{\sigma}_2 + \hat{\sigma}_3)^2 - \frac{\hat{\sigma}_2 \hat{\sigma}_3}{S_T^2} = 1.0 \\ A_{mc}(\hat{\sigma}_2) + B_{mc}(\hat{\sigma}_2)^2 = 1.0 \end{cases} \Leftrightarrow \begin{cases} -2\hat{\sigma} A_{mc} + 4\hat{\sigma}^2 B_{mc} - \frac{\hat{\sigma}^2}{S_T^2} = 1.0 \\ -Y_c A_{mc} + Y_c^2 B_{mc} = 1.0 \end{cases} \quad (26)$$

Since the system of equations has three unknowns and only two equations these cannot be solved directly, but using the assumption that in biaxial compression $\sigma_2 = \sigma_3 = -\sigma \gg Y_c$, it can be admitted the following limit (27). Using this limit, it is possible to calculate the rest of unknown matrix compressive parameters for a closed envelope surface, as long as that $Y_c > 2S_T$. Therefore, it is possible to assemble the compressive matrix failure criterion (28).

$$\lim_{\sigma \rightarrow \infty} \Rightarrow B_{mc} = \frac{1}{4S_T^2} \Leftrightarrow A_{mc} = \frac{\frac{Y_c^2}{4S_T^2} - 1}{Y_c} \quad (27)$$

$$F_{mc} = \left[\left(\frac{Y_c}{2S_T}\right)^2 - 1\right] \left(\frac{\hat{\sigma}_2 + \hat{\sigma}_3}{Y_c}\right) + \left(\frac{\hat{\sigma}_2 + \hat{\sigma}_3}{2S_T}\right)^2 + \frac{\hat{t}_{23}^2 - \hat{\sigma}_2 \hat{\sigma}_3}{S_T^2} + \frac{\hat{t}_{21}^2 + \hat{t}_{31}^2}{S_L^2} \leq 1.0 \quad \text{if } \hat{\sigma}_2 + \hat{\sigma}_3 < 0 \quad (28)$$

The condition of matrix tensile and compressive behaviour is demonstrated in the work of [Hashin 80], and its using proof by contradiction, in which is the only condition that does not violate the principal of $\hat{\sigma}_2 \geq 0; \hat{\sigma}_3 \geq 0$ in all quadrants of the space $\hat{\sigma}_2 - \hat{\sigma}_3$.

For the interlaminar failure criterion, a cohesive model (29) is used for tensile interlaminar failure criterion, based on the initial work of [21] with influence of the shear stresses in the interlaminar plane (30). For the interlaminar compressive failure, the influence of the shear is minor, therefore, for this case

only the pressure stresses is taken into account for the failure criterion (30). Z_t and Z_c are the out-of-plane damage tensile and compressive thresholds respectively.

$$\left(\frac{\sigma_{nn}}{\sigma_t}\right)^2 + \left(\frac{\tau_{nt}}{S_T}\right)^2 + \left(\frac{\tau_{nl}}{S_L}\right)^2 \leq 1.0 \quad (29)$$

$$\begin{aligned} F_{it} &= \left(\frac{\hat{\sigma}_3}{Z_t}\right)^2 + \left(\frac{\tau_{31}}{S_L}\right)^2 + \left(\frac{\tau_{32}}{S_T}\right)^2 \leq 1.0 \quad \text{if } \hat{\sigma}_3 \geq 0 \\ F_{ic} &= \left(\frac{\hat{\sigma}_3}{Z_c}\right)^2 \leq 1.0 \quad \text{if } \hat{\sigma}_3 < 0 \end{aligned} \quad (30)$$

4.2 Damage Evolution

For this work the same formulation of equivalent strains and stresses used in previous 2D Hashin damage models is used [15]. These are then updated and assembled for the 3D space using the same MLT principals [11], with different equivalent stresses and strains for the fibre, matrix and interlaminar in tensile and compressive damage evolution [47].

The equivalent strain is calculated using general equivalent principal virtual work [48], written in the form of (31). For the particular cases of the fibre and matrix directions, these equations are rewritten into (32), (33). The chosen stresses and strains used to compute the equivalent ones, are associated with the effective stresses present in the respective failure criterion.

$$\sigma_{eq}\varepsilon_{eq} = \sum \sigma_{ij}\varepsilon_{ij} \quad \text{and} \quad \varepsilon_{eq} = \sqrt{\sum \varepsilon_{ij}^2} \quad (31)$$

$$\begin{cases} \varepsilon_{eq,ft} = \sqrt{\langle \varepsilon_1 \rangle^2 + \gamma_{12}^2 + \gamma_{13}^2} \\ \varepsilon_{eq,fc} = \langle -\varepsilon_1 \rangle \\ \varepsilon_{eq,mt} = \sqrt{\langle \varepsilon_2 \rangle^2 + \langle \varepsilon_3 \rangle^2 + \gamma_{21}^2 + \gamma_{23}^2 + \gamma_{31}^2} \\ \varepsilon_{eq,mc} = \sqrt{\langle -\varepsilon_2 \rangle^2 + \langle -\varepsilon_3 \rangle^2 + \gamma_{21}^2 + \gamma_{23}^2 + \gamma_{31}^2} \\ \varepsilon_{eq,it} = \sqrt{\langle \varepsilon_3 \rangle^2 + \gamma_{31}^2 + \gamma_{32}^2} \\ \varepsilon_{eq,ic} = \langle -\varepsilon_3 \rangle \end{cases} \quad (32)$$

$$\begin{cases} \sigma_{eq,ft} = \frac{\langle \sigma_1 \rangle \langle \varepsilon_1 \rangle + \tau_{12}\gamma_{12} + \tau_{13}\gamma_{13}}{\sqrt{\langle \varepsilon_1 \rangle^2 + \gamma_{12}^2 + \gamma_{13}^2}} \\ \sigma_{eq,fc} = \langle -\sigma_1 \rangle \\ \sigma_{eq,mt} = \frac{\langle \sigma_2 \rangle \langle \varepsilon_2 \rangle + \langle \sigma_3 \rangle \langle \varepsilon_3 \rangle + \tau_{21}\gamma_{21} + \tau_{23}\gamma_{23} + \tau_{31}\gamma_{31}}{\sqrt{\langle \varepsilon_2 \rangle^2 + \langle \varepsilon_3 \rangle^2 + \gamma_{21}^2 + \gamma_{23}^2 + \gamma_{31}^2}} \\ \sigma_{eq,mc} = \frac{\langle -\sigma_2 \rangle \langle -\varepsilon_2 \rangle + \langle -\sigma_3 \rangle \langle -\varepsilon_3 \rangle + \tau_{21}\gamma_{21} + \tau_{23}\gamma_{23} + \tau_{31}\gamma_{31}}{\sqrt{\langle -\varepsilon_2 \rangle^2 + \langle -\varepsilon_3 \rangle^2 + \gamma_{21}^2 + \gamma_{23}^2 + \gamma_{31}^2}} \\ \sigma_{eq,it} = \frac{\langle \sigma_3 \rangle \langle \varepsilon_3 \rangle + \tau_{31}\gamma_{31} + \tau_{32}\gamma_{32}}{\sqrt{\langle \varepsilon_3 \rangle^2 + \gamma_{31}^2 + \gamma_{32}^2}} \\ \sigma_{eq,ic} = \langle -\sigma_3 \rangle \end{cases} \quad (33)$$

To alleviate mesh dependency that may occur with material softening, a characteristic length L_c is introduced into the formulation, so that the constitutive law is expressed as a stress-equivalent displacement relation [12]. In this work, it is considered that the characteristic length is computed as the square root of the numerically computed surface area. The equivalent displacement definitions (34) are the same as the ones initially found in the work of [49], which do not depend on the crack direction. This last statement is even more important in orthotropic damage models, since the damage evolution will always depend on either the fibre or matrix behaviour. It has been demonstrated in several works, if the mesh is not regular and the stress field distribution is non-uniform, that some element dependency/sensitivity is predictable as a consequence of FEM with softening [12,50].

The “evolution law” is then rewritten, and takes the final form represented in Figure 1, in which the area $\widehat{ABC} \Rightarrow (\varepsilon_{eq}(d = 0))$ under the curve corresponds to the fracture energy $G_{f,m}$. At the moment new experimental methodologies exist to calculate fracture energy [51], but for orthotropic materials the classical Compact Tension test is still suggested.

The initial values σ_{eq}^0 and δ_{eq}^0 are calculated in the onset of damage, by analytically solving equations (23), (25), (28) and (30). In order to obey the Kuhn-Tucker equations, after the beginning of each incremental process, the “evolution law” is updated to curve $\widehat{ADC} \Rightarrow (\varepsilon_{eq}(d))$.

After the damage initiation criteria, beyond point B , it is demonstrated in [11], for a linear softening evolution, that the damage variables are calculated according to equation (35), depending on fibre or matrix and on tension or compression.

$$\delta_{ij}^{eq} = L_c \varepsilon_{ij}^{eq} \quad \text{and} \quad \delta_{eq}^u = 2G_f / \sigma_{eq} \quad (34)$$

$$d = \frac{\delta_{eq}^u (\delta_{eq} - \delta_{eq}^0)}{\delta_{eq} (\delta_{eq}^u - \delta_{eq}^0)} \quad \text{if} \quad \delta_{eq}^0 \leq \delta_{eq} \leq \delta_{eq}^u \quad (35)$$

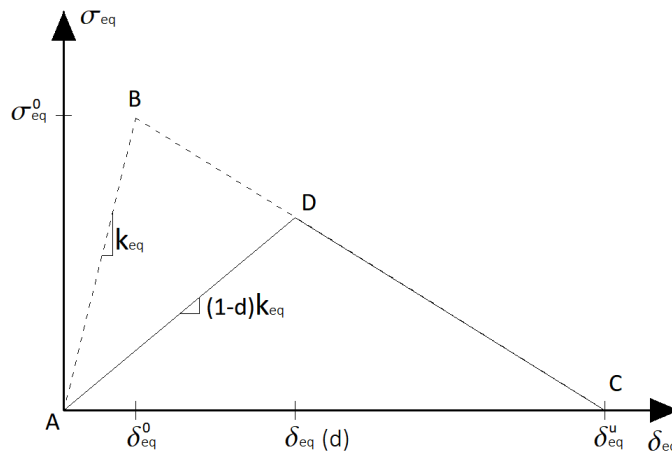


Figure 1 – Constitutive relation for the equivalent stress and equivalent displacement.

In this work it is also adopted the possibility of the equivalent stresses present a residual stress, this is important mainly when compression is high and very present in the structural response. Also to promote some numerical stability is recommended the use a tensile residual stress that may vary from 1% to 10% of its initial peak value. The adopted residual equivalent stress formulation in Figure 2 is adopted. A new damage function is assembled, during the residual equivalent stress segment after point D (37).

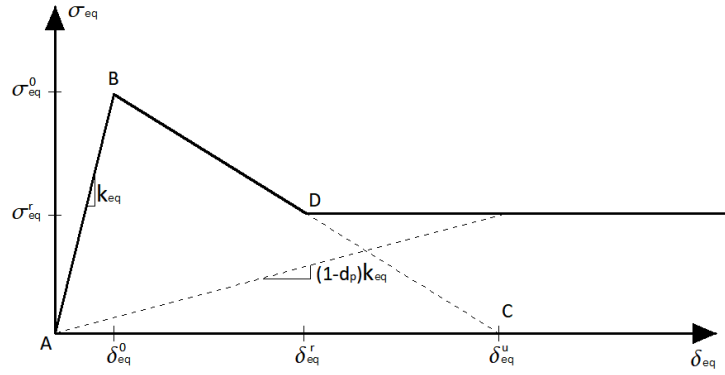


Figure 2 – Constitutive relation with residual stress for the equivalent stress and equivalent displacement.

$$\begin{cases} \sigma_{eq}^r = (1 - d_D)k_{eq}\delta_{eq}^D = (1 - d_D)\frac{\delta_{eq}^D}{\delta_{eq}^0}\sigma_{eq}^0 = \% \sigma_{eq}^0 \\ (1 - d_D) = \frac{\delta_{eq}^0(\delta_{eq}^u - \delta_{eq}^D)}{\delta_{eq}^D(\delta_{eq}^u - \delta_{eq}^0)} \end{cases} \Rightarrow \delta_{eq}^D = \delta_{eq}^u - \%(\delta_{eq}^u - \delta_{eq}^0) \quad (36)$$

$$\begin{aligned} \sigma_{eq} &= (1 - d_r)k_{eq}\delta_{eq} = \sigma_{eq}^r = \% \sigma_{eq}^0 \\ \Leftrightarrow (1 - d_r)\frac{\sigma_{eq}^0}{\delta_{eq}^0}\delta_{eq} &= \% \sigma_{eq}^0 \\ \Leftrightarrow d_r &= 1 - \% \frac{\delta_{eq}^0}{\delta_{eq}} \end{aligned} \quad (37)$$

4.3 Viscous Regularization

When using only the energy regularization described in the previous section, some issues are still left that may cause: (i) loss of positive definiteness of the tangent stiffness; (ii) some localization of damage; and (iii) some numerical convergence difficulties. To overcome these problems, an efficient/simple procedure is to implement a viscous regularization.

When the tangent stiffness tensor is not positive definite, damage localizes in a narrow band, and the numerical solution depends upon the numerical discretization: decreasing the element size in the localized zone decreases the computed energy dissipated. Therefore, the structural response is not objective because it does not converge to a unique solution with mesh refinement. Also when the tangent stiffness is not positive definite, standard Newton-Raphson techniques present convergence difficulties [52].

As referred above, it is possible to overcome some of these convergence difficulties by using the viscous regularization scheme. This numerical algorithm is based on an artificial Duvaut-Lions viscosity model [53]. More details on the theoretical background of this method can be found in the work of [54]. This algorithm causes the tangent stiffness matrix of the softening material to be positive definite for sufficiently small time increments, improving the convergence. In this regularization scheme a viscous damage variable is defined by the evolution equation (38).

$$\delta d_v = \frac{1}{\eta}(d - d_v) \times \delta_t \quad (38)$$

Where d is the damage variable obtained as described previously, d_v is the regularized viscous damage variable, and η is the viscosity stabilization factor. The damage response of the viscous material is given as (39) and the non-damage response is give as (40).

$$\{\sigma_v\} = [C_d^v]\{\varepsilon\} \quad (39)$$

$$\{\sigma\} = [C_d]\{\varepsilon\} \quad (40)$$

The damaged elastic matrix, C_d^v , is computed using viscous values of damage variables for each failure mode. Using viscous regularization with a small value for the viscosity parameter (small compared to the characteristic time increment) usually helps improving the rate of convergence of the model in the softening regime, without compromising the quality of the numerical solution. The basic idea is that the solution of the viscous system relaxes to that of the inviscid case as $\eta \rightarrow 0$, where t represents time. A numerical algorithm needs to be implemented for the time integration of the internal variables. Using a backward-Euler scheme [55], the internal variables can be updated, resulting in the viscous damage variable (41), by combining it with the previous expression (38).

$$d_v^{t+\Delta t} = d_v^t + \Delta d_v^t \Rightarrow d_v^{t+\Delta t} = d_v^t + \frac{1}{\eta} (d^{t+\Delta t} - d_v^{t+\Delta t}) \times \Delta t \quad (41)$$

It is now possible to compute the viscous damage, using the information from the previous viscous damage, and the current non-viscous damage (42), retaining the implicit time integration.

$$d_v^{t+\Delta t} = \frac{\eta}{\eta + \Delta t} d_v^t + \frac{\Delta t}{\eta + \Delta t} d^{t+\Delta t} \quad (42)$$

It is important to guarantee that level of viscosity is not that high, that is performed indirectly by comparing the level of elastic damaged energy (43), and the viscous energy dissipation (44), in which the first must always override the second. If the time step Δt if very small, it is possible that the first term of the sum in (44) overrides the second, providing an increase of viscous energy dissipation, that may compromises the accuracy of the results.

$$E_d^{t+\Delta t} = E_d^t + \frac{1}{2} \left[\sum_{i=1}^n (\sigma_{v,i}^{t+\Delta t} + \sigma_{v,i}^t) \Delta \varepsilon_i \right] \quad (43)$$

$$E_v^{t+\Delta t} = E_v^t + \frac{1}{2} \left[\sum_{i=1}^n (\sigma_{v,i}^{t+\Delta t} + \sigma_{v,i}^t - \sigma_i^{t+\Delta t} - \sigma_i^t) \Delta \varepsilon_i \right] \quad (44)$$

5 Proposed Predictor-Corrector Implicit to Explicit

Many authors have user UMAT user-subroutines in ABAQUS without resourcing to a fully Jacobi stiffness matrix (aka tangent matrix). Most authors even supress this information in their publications, using only a secant matrix for ABAQUS predictor-corrector, with viscous regularization.

As referred before, viscous regularization was only been demonstrated to be a fully implicit method, when a tangent matrix is used for the predictor-corrector [56,54]. The use of secant matrix with viscous regularization lacks theoretical background to prove its implicit convergence. It can be seen in expression

(42), that the if the time step is larger than viscosity parameter $\Delta t \gg \eta$, then the level of regularization is low enough, and the implicit standard convergence can be admitted, since the viscous damage is always related to the current time step as the non-viscous damage. However, if the time step is lower than the viscosity parameter $\Delta t \ll \eta$ then the viscous damage will always be related to the previous time step, therefore, promoting and explicit time step integration.

This last case can cause some conflicts, since the strain increment follows a full implicit integration scheme (45). These inconsistencies happen when damage follows an explicit time step update $d_v^{t+\Delta t} \simeq d_v^t$, and the strain increment follows a full implicit integration scheme. This can cause some convergence problems, especially if the time step is very small $\Delta t \ll \eta$. Also, when the time step is very small since the viscous damage solution overrides the non viscous damage solution, the viscous damage energy tends to grow (44), indirectly providing an extra energy that it is not real.

$$\varepsilon_{t+\Delta t} = \varepsilon_t + \Delta \varepsilon_{t+\Delta t} \quad (45)$$

To solve this problem, a new implicit to explicit algorithm is proposed, in which the fundamental basis guarantees that when the time step is large, the damage evolution follows an implicit time step integration, but when the time step is smaller than the viscosity parameter, then the damage evolution switches to an explicit time step integration. This is an optimization of the predictor-corrector of ABAQUS, that states when the time step is large enough a full implicit formulation is used, but when the predictor-corrector algorithm of ABAQUS presents complications in converging reducing the time step then an explicit formulation is used to suppress the converging difficulty. The basis of this formulation is using increment correction parameter ϖ linked to the portion of the non-viscous damage variable $d^{t+\Delta t}$ in expression (46).

$$\varepsilon_{t+\Delta t} = \varepsilon_t + \varpi \times \Delta \varepsilon_{t+\Delta t} \quad (46)$$

In which:

$$\varpi = \frac{\Delta t}{\Delta t + \eta} \quad (47)$$

It is important to point out that when $\varpi = 1.0$ the material stiffness and stress update during the time integration in the UMAT follows a full implicit formulation, on the contrary when $\varpi = 0.0$ it follows a full explicit time integration for the material stiffness and stress update.

Using this algorithm it is guaranteed that when performing the viscous regularization, that if the predictor-corrector uses large time steps, than both the viscous and non-viscous solution portion of expression (42) will contribute for the implicit time step integration. But, when the time step is small enough, then the increment correction parameter tends to be small, close to an explicit integration, and the influence of the non-viscous solution overrides the viscous solution, therefore using only the previous damage variable. This way there is no mixed implicit time step integration, with previous step damage variables, as suggested before may compromise the convergence and accuracy of the numerical solution.

To better understand the variation of ϖ with Δt for a fixed $\eta = 10^{-5}$, it is depicted in Figure 3 a) a graph, in which it is possible to see that even for small times steps from $\Delta t = 10^{-3}$ to $\Delta t = 10^{-5}$, the value of $\varpi > 50\%$, therefore guaranteeing some influence of the $\Delta \varepsilon_{t+\Delta t}$ in the final strain increment $\varepsilon_{t+\Delta t}$. This does not assure a full implicit behaviour, but close to it. As depicted in Figure 3 b) using logarithmic scale only when the $\Delta t < 10^{-6}$ the value of $\varpi < 10\%$, being near an explicit form, but still with some influence of $\Delta \varepsilon_{t+\Delta t}$ in the final strain increment $\varepsilon_{t+\Delta t}$.

In conclusion the algorithm tends to be more implicit, when $\Delta t > \eta$, and on the other hand more explicit when $\Delta t < \eta$. In any case, this last situation is non problematic, since for very small time steps $\Delta t \ll 10^{-6}$, an explicit solution may still provide good and accurate numerical results. It is important to state, that this algorithm admits the damage variable from the current time step $d^{t+\Delta t}$ is always saved for the next time step, otherwise viscous damage non-viscous damage would never be updated, during the incremental processes.

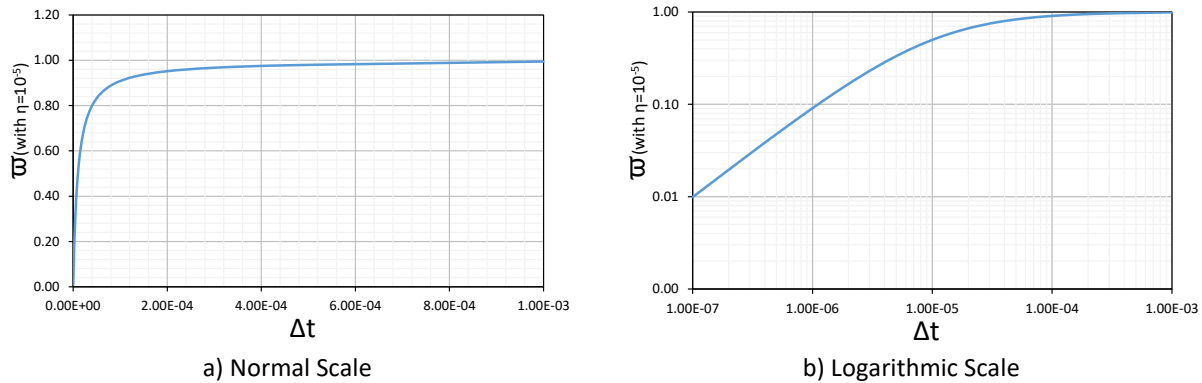


Figure 3 – Constitutive relation with residual stress for the equivalent stress and equivalent displacement.

It is important to point out, that expression (46) is only use to update the damage variables, however for the stress update, expression (45) is always used even for explicit integration if not the internal forces wouldn't be in equilibrium.

6 Numerical Tests

In this section the results from the experimental campaign of [57], [58] and [59] with GFRP specimens, beams and connections are tested and compared with the proposed damage model and the stabilization algorithm. These experimental results are fundamental to validate numerical models, since they present most of the material properties including fracture energy, which is fundamental for correctly simulate numerically the post peak behaviour in materials with softening. Most of these experimental campaigns have also been verified with previous numerical tests in the works of [60,61].

For numerical tests it was admitted a total time analysis of 1.0 seconds, due to the non-linear analysis being static, and all time step increments should have a minimum of 0.001 seconds, which is 100 times bigger than the adopted viscosity parameter.

6.1 Compact Tension Test

The compact tension test, is a traditional test to inquirer fracture energy usually in isotropic metals [62], and recently extended to also estimate the fracture energy in orthotropic GFRP specimens [58]. A full detail of the experimental campaign for the tensile compact test can be found at [58], including the description of the impose displacement in the test setup.

The specimen geometry, test setup and supporting conditions are all depicted in Figure 4. For the adopted mesh, to reduce the computational cost, the zone outside the notch was modelled with linear orthotropic GFRP behaviour that already existed in ABAQUS material library. The extra part of the notch was simulated with the proposed UMAT, in which the fracture will occur. These two used different

meshes, since the zone in the notch needs an extra refinement, and later were connected using tie constraints. The circular supports were modelled with linear isotropic steel also presented in ABAQUS material library ($E_s = 195\text{GPa}$, $\nu = 0.3$). The contact between the supports and the GFRP specimen was simulated with hard contact formulation, and with a friction coefficient of 0.2.

To reduce even further the computational cost, only half of the thickness was simulated, therefore a transversal symmetry conditions was implemented Figure 5. When the mesh was generated, it was imposed geometries near cubes for all solid finite elements, and several meshes were tested to prevent any mesh dependency.

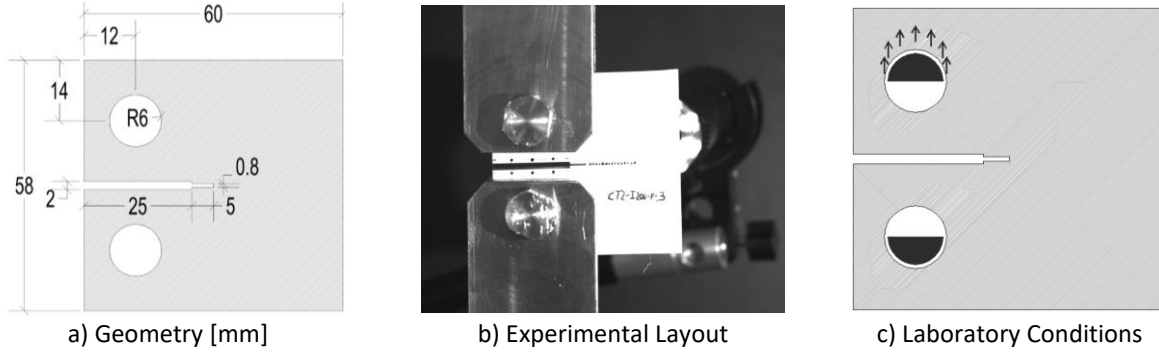


Figure 4 – Geometry and test setup for the classical compact tension test (CT) [58].

A full 3D non-linear analysis was performed using ABAQUS standard with C3D8 solid finite elements using full integration and hourglass control. It was observed during the previous experimental campaign, that the structural response produced softening, therefore displacement control was used during the applied vertical load. All the materials properties in plane 1-2 of the GFRP are in Table 1 and Table 2, and these were obtained in the experimental campaign of [58]. For the interlaminar material properties it was admitted the same as the matrix properties, due to some isotropic behaviour in the transverse direction.

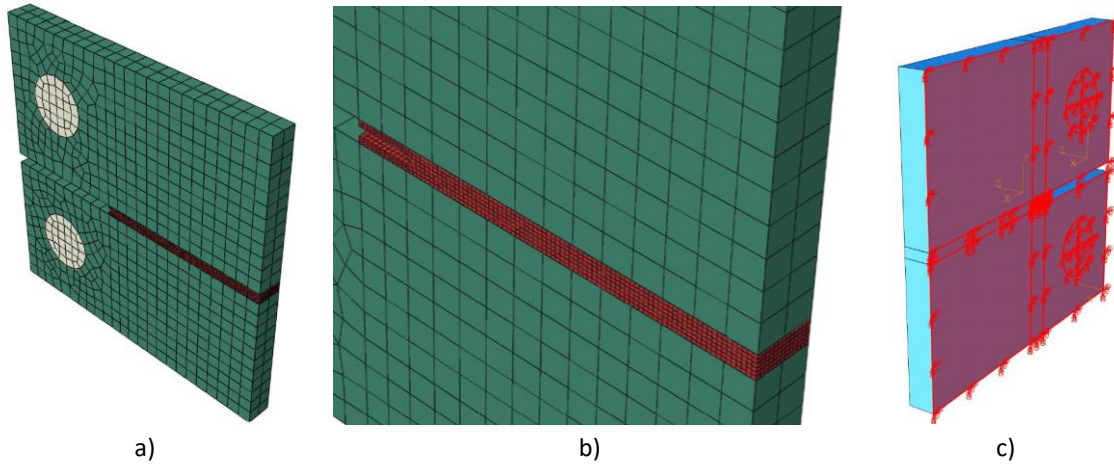


Figure 5 – Adopted 3D mesh and symmetry conditions for the CT test.

Table 1 – Materials Properties for the pultruded GFRP material used in the CT tests.

$E_1[\text{MPa}]$	$E_2[\text{MPa}]$	$E_3[\text{MPa}]$	$G_{12}[\text{MPa}]$	$G_{13}[\text{MPa}]$	$G_{23}[\text{MPa}]$
29600	11900	11900	2900	3000	3000
$\nu_{12}[-]$	$\nu_{13}[-]$	$\nu_{23}[-]$	$X_t[\text{MPa}]$	$X_c[\text{MPa}]$	$Y_t[\text{MPa}]$
0.27	0.27	0.30	323	426	71
$Y_c[\text{MPa}]$	$Z_t[\text{MPa}]$	$Z_c[\text{MPa}]$	$S_L[\text{MPa}]$	$S_T[\text{MPa}]$	$\eta[-]$
121	71	121	64	67	10^{-5}

Table 2 – Fracture energy for the pultruded GFRP material used in the CT tests.

G_{ft} [MPa.mm]	G_{fc} [MPa.mm]	G_{mt} [MPa.mm]	G_{mc} [MPa.mm]	G_{it} [MPa.mm]	G_{ic} [MPa.mm]
100	100	20	20	20	20

Three different tests were performed to evaluate the numerical accuracy of the new proposed algorithm: the 1st test consists on a full implicit material integration with correction parameter $\varpi = 1.0$; the 2nd test consists on a full explicit material integration considering $\varpi = 0.0$; the 3rd test is using ITE with the correction parameter of expression (47). It is important to point out, that the UMAT was used for the GFRP, using ABAQUS standard, so the governing system was solved using implicit predictor-correct algorithm for the three tests.

By observing Figure 6, it is important to realize that all three tests provided the same structural response, even during the softening branch. The stiffness is the same in all three tests, but the maximum force is slightly higher in the 2nd test (explicit) as expected. All numerical models present higher maximum force than the experimental campaign, but this is also observed from other authors [63]. Also in Figure 7 it is displayed the matrix damage and vertical stress distribution for a given vertical strain. For the matrix damage evolution both three tests present the same evolution with the vertical strain, but for the vertical stress evolution during the peak, there is a clear difference between the implicit and explicit material integration (1st and 3rd test respectively). But for the evolution of the vertical stress and vertical strain, there is almost no visible difference between the implicit and ITE material integration, concluding that the ITE promotes the same accuracy as the full implicit formulation. It is also presented in Figure 7 the final matrix damage field distribution for all the three numerical tests, in which it is not possible to inquire the differences between each of the material time integration methods.

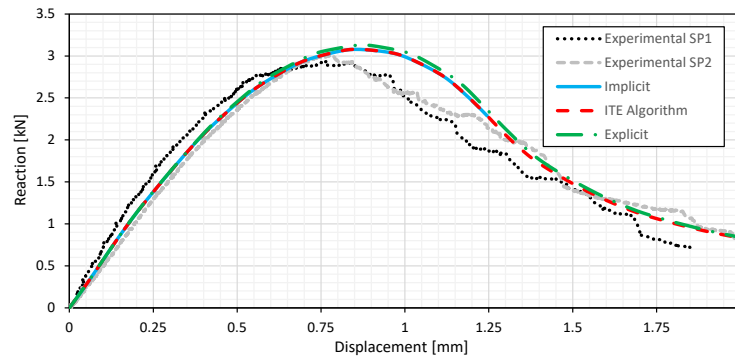


Figure 6 – Vertical force vs displacement, in the load supports for the CT test.

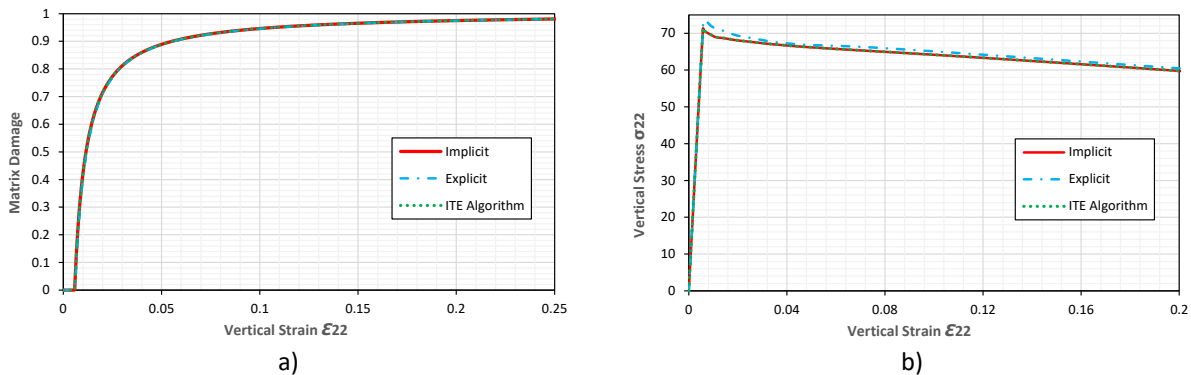


Figure 7 – a) damage vs vertical strain, b) vertical stress vs vertical strain, for the CT test.

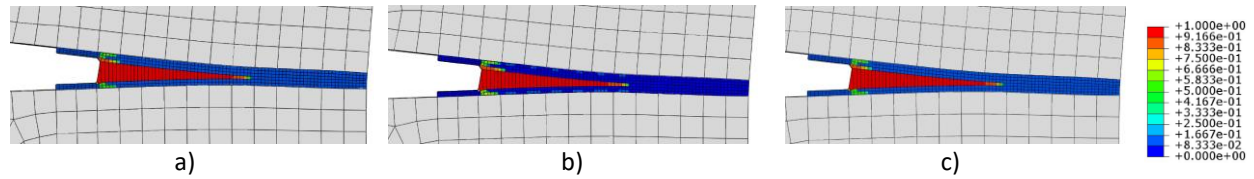


Figure 8 – Final matrix damage field distribution for a) implicit, b) explicit and c) ITE, for the CT test.

6.2 Three Point Bending Beam

The three point bending beam is an experimental study commonly used to extract fracture properties of materials. The experimental setup details are presented in [59], in which a bilinear softening relation describes the mechanical behaviour of damaged pultruded glass fiber reinforced polymer (GFRP) composites. Based on the previous referenced work, the material properties adopted for the numerical test are listed in Table 3. Table 4 contains the fracture energies adopted in this framework. For the sake of clarity, tensile and compressive values of fracture energies for the fiber are estimated, while an average value of bilinear behaviour is taken into consideration for the matrix. Moreover, interlaminar fracture energy is assumed to be the same as the matrix property.

The computational cost is reduced by considering only one quarter of the beam, thus requiring symmetry conditions, as illustrated in Figure 9. As regards the boundary conditions, the beam is simply supported and the vertical displacement is applied through an isotropic steel support ($E_s = 210 \text{ GPa}$, $\nu = 0.3$), according to [61]. The part of the beam far from the notch proposes a coarse discretization and it is modelled with linear orthotropic behaviour, in contrast to the region of the notch where the damage occurs, which is modelled using almost cubic C3D8R solid finite elements with reduced integration and hourglass control, as shown in Figure 10. Tie constraints allow the connection between all the parts of the beam.

Table 3 – Materials Properties for the pultruded GFRP material used in the CT tests.

$E_1 [\text{MPa}]$	$E_2 [\text{MPa}]$	$E_3 [\text{MPa}]$	$G_{12} [\text{MPa}]$	$G_{13} [\text{MPa}]$	$G_{23} [\text{MPa}]$
30000	10800	10800	2000	2000	2000
$\nu_{12} [-]$	$\nu_{13} [-]$	$\nu_{23} [-]$	$X_t [\text{MPa}]$	$X_c [\text{MPa}]$	$Y_t [\text{MPa}]$
0.24	0.24	0.4	323	423	37
$Y_c [\text{MPa}]$	$Z_t [\text{MPa}]$	$Z_c [\text{MPa}]$	$S_L [\text{MPa}]$	$S_T [\text{MPa}]$	$\eta [-]$
80	37	80	33	33	10^{-5}

Table 4 – Fracture energy for the pultruded GFRP material used in the three point bending beam.

$G_{ft} [\text{MPa} \cdot \text{mm}]$	$G_{fc} [\text{MPa} \cdot \text{mm}]$	$G_{mt} [\text{MPa} \cdot \text{mm}]$	$G_{mc} [\text{MPa} \cdot \text{mm}]$	$G_{it} [\text{MPa} \cdot \text{mm}]$	$G_{ic} [\text{MPa} \cdot \text{mm}]$
130	130	3.84	3.84	3.84	3.84

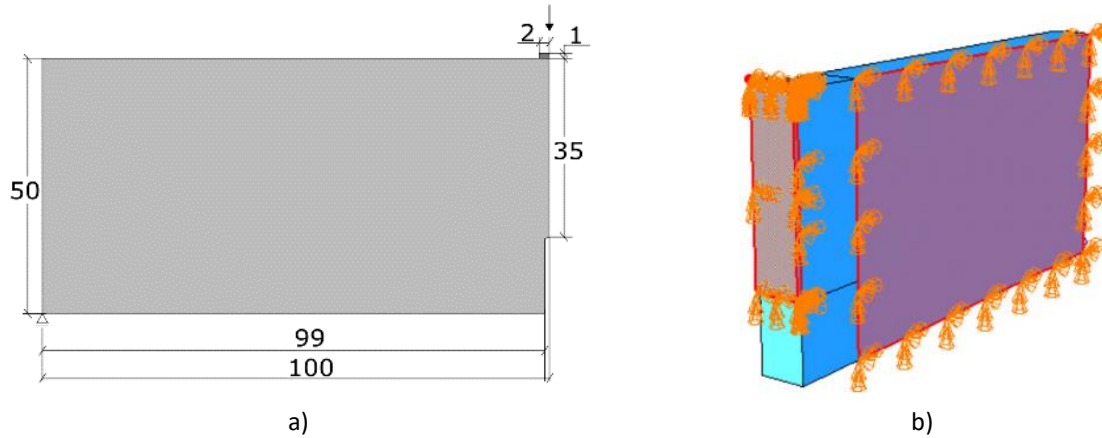


Figure 9 – Geometry and symmetric boundary conditions of the beam.

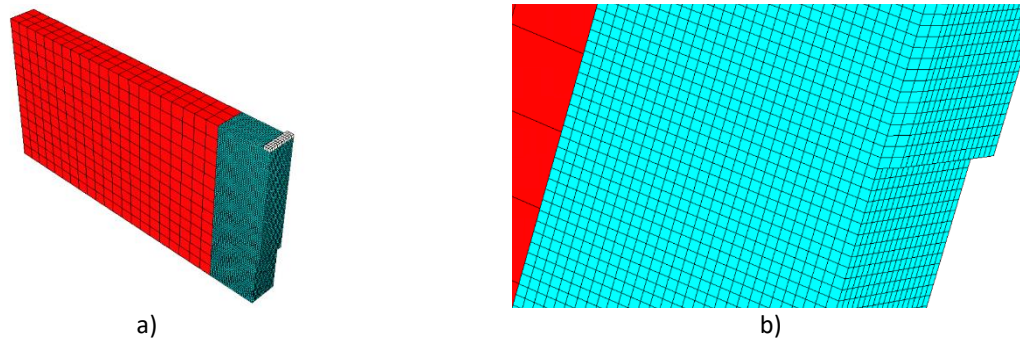


Figure 10 – Adopted 3D mesh for the three point bending beam.

A full 3D non-linear analysis was performed using ABAQUS standard, without considering residual stress and with the same time step restrictions as the previous numerical model. This framework proposes a full implicit material integration as 1st analysis, followed by ITE test with the correction parameters defined in (47) as 2nd test.

The response of the structure in terms of reaction force vs CMOD is compared with the experimental data included in [Liu et al. 2017], as illustrated in Figure 11. By considering both full implicit and ITE tests, Figure 12 b) exhibits the evolution of principal stress over two different integration points, identified in Figure 12 a), in the band where the damage propagates. A detailed view of damage propagation is provided in Figure 13; matrix, Figure 13 a), and fiber, Figure 13 c), tensile damages can be recognized, while Figure 13 b) shows shear 1-2 damage progression. Finally, Figure 14 compares the final distribution of tensile matrix damage using full implicit material integration and ITE algorithm. The numerical assessment correctly simulates the experimental campaign, even though some differences in the softening region can be detected. In particular, the numerical model contains an average value of matrix fracture energy in contrast to the bilinear behaviour. Also, the reduced integration results in a smaller characteristic length. In addition, small inconsistencies between experimental and numerical boundary conditions could induce some variabilities. As portrayed in Figure 12 b), principal stress and strain obtained from full implicit case and ITE are coincident. Therefore, ITE algorithm simulates the mechanical response of the beam with the same accuracy as full implicit analysis. The matrix damage over integration point 2 evolves more rapidly than point 1. However, by looking at Figure 13 c), there is an increase in fiber

damage that causes the shear damage at point 1 to exceed that at point 2 from the cross point, as highlighted in Figure 13 b).

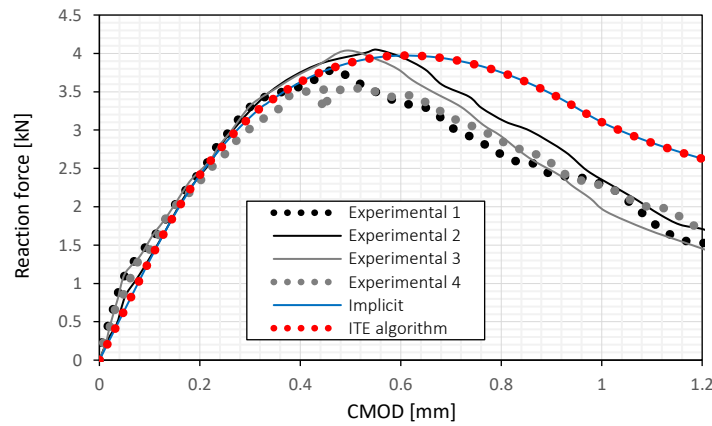


Figure 11 – Vertical reaction force vs CMOD for implicit and ITE.

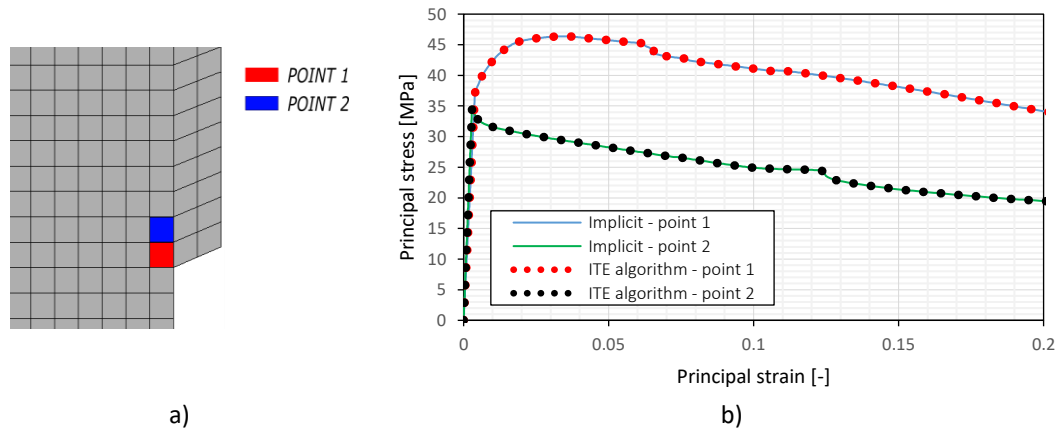
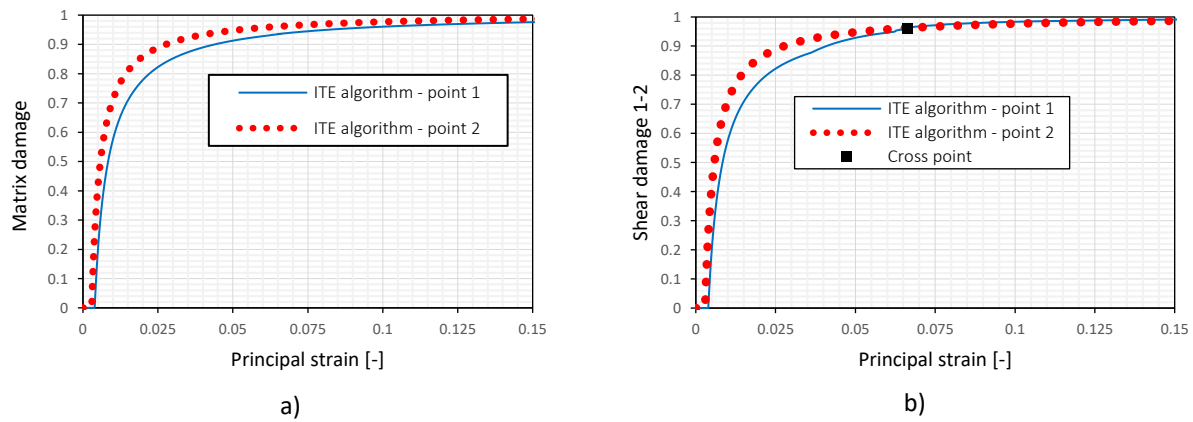
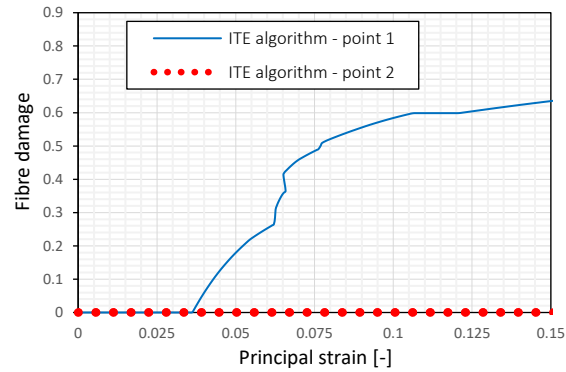


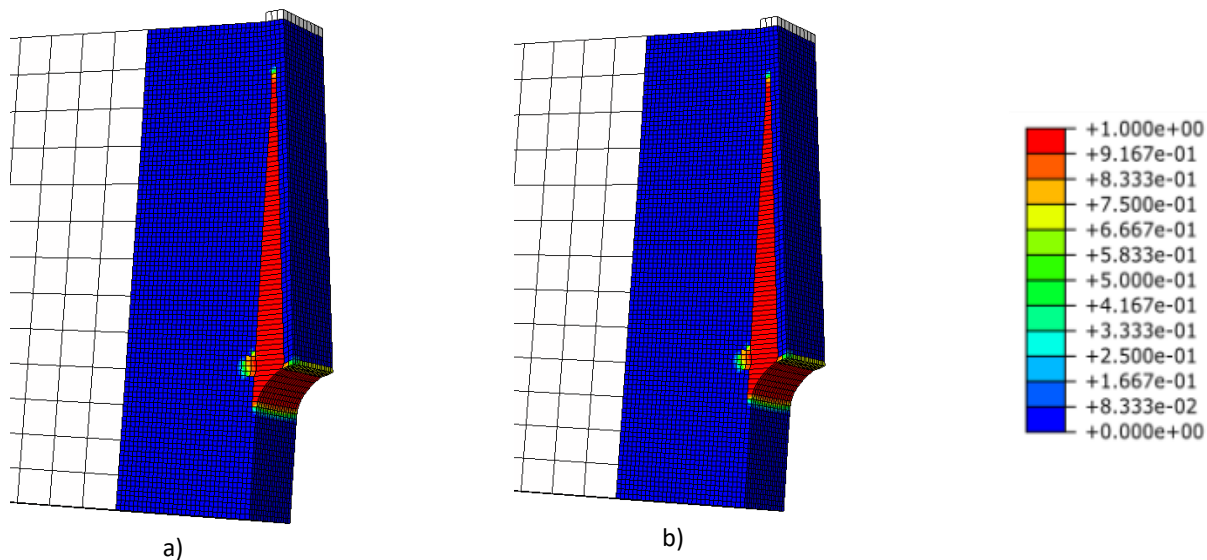
Figure 12 – Principal stress vs principal strain for implicit and ITE on points 1 and 2 in the damaged band.





c)

Figure 13 – Tensile a) matrix damage, b) shear damage and c) tensile fiber damage field distributions over integration points 1 and 2 with ITE algorithm.



a)

b)

Figure 14 – Final tensile matrix damage distribution for a) implicit and b) ITE.

6.3 Double Lap Test

The double lap test is a standard experiment use to assess the bolt connection between structural elements. The full detail of the experimental campaign and test setup is fully described in the work of [57], in which it is possible to see the applied load using impose displacements. Some of the material properties adopted for the numerical test are in Table 5, and these were obtained in the previous referenced work, others were estimated. For the fracture energy, due to some variability in the results, it was used the same values of the previous numerical tests in Table 2. For this numerical test, the bolt edge distance (cover) of 15mm and 70mm were simulated, since these clear show a difference between a shear-out and bearing collapse respectively Figure 15.

A full 3D non-linear analysis was performed using ABAQUS standard with C3D8 and C3D8R solid finite elements using full and reduce integration and hourglass control, to evaluate any mesh sensitivity due to the high variability of the stress field. The time step restrictions are the same as the previous numerical models.

For the GFRP plate, in order to reduce the computational cost, part of the plate near the opening was modelled with the UMAT, but for the other part it was used an elastic orthotropic material from ABAQUS library. For the steel bolt an isotropic elastoplastic material from ABAQUS library was used ($E_s = 195GPa$, $\nu = 0.3$, $f_y = 300MPa$, $f_u = 691MPa$). Again to reduce the computational cost, only $\frac{1}{4}$ of the structure was simulated, which means $\frac{1}{2}$ of the GFRP plate and one steel plate Figure 16, in which the impose vertical displacement is inserted in the bottom of the steel plate. For this example only the ITE algorithm was used, in which the main purpose is to numerically assess the simulation of the bearing collapse in the contact between the steel bolt and the GFRP plate.

To correctly simulate the bearing, the residual compressive stress after the maximum peak must also be simulated. Two values of compressive residual stress were considered 15% estimated from the work of [60] and 80% which is approximately the relation between the bearing resistance and compressive resistance according to [64], when using the experimental values form [57]. Also to improve convergence the tensile residual stress was 1% and 10% respectively. A sensitivity test, shown that a residual tensile stress below 15% had no influence in the maximum numerical resistance and its softening branch.

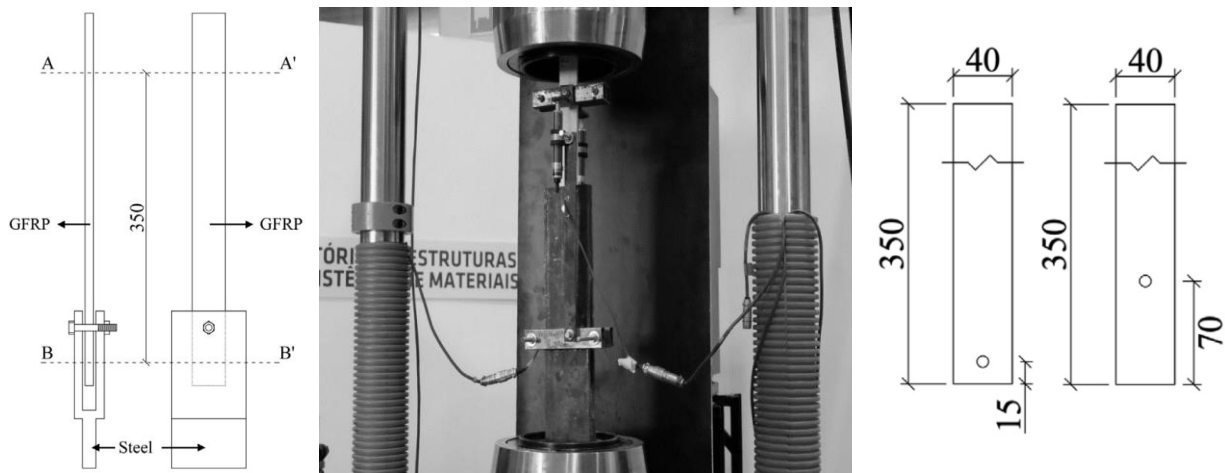


Figure 15 – Test setup for the loading conditions and impose displacement for the double lap test, and used bolt edge distance (cover) for the circular opening [57].

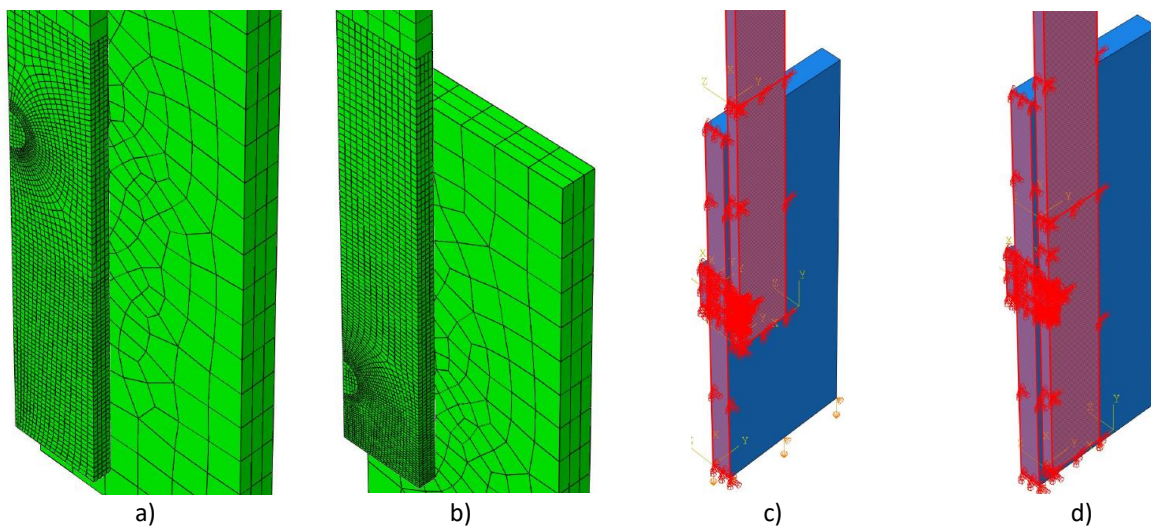


Figure 16 – Adopted 3D mesh and symmetry conditions for the double lap test.

Table 5 – Materials Properties for the pultruded GFRP material used in the double lap tests.

E_1 [MPa]	E_2 [MPa]	E_3 [MPa]	G_{12} [MPa]	G_{13} [MPa]	G_{23} [MPa]
21300	2900	2900	3000	2500	2500
ν_{12} [-]	ν_{13} [-]	ν_{23} [-]	X_t [MPa]	X_c [MPa]	Y_t [MPa]
0.28	0.28	0.30	334.0	316.0	29.0
Y_c [MPa]	Z_t [MPa]	Z_c [MPa]	S_L [MPa]	S_T [MPa]	η [-]
51.9	29.0	51.9	52.4	33.8	10 ⁻⁵

The structural response of the numerical models and its comparison with the experimental campaign are exhibited in Figure 17 for both 15mm and 70mm cover, with 15% and 80% residual compressive strength, for both reduce (red) and full (full) integration. The vertical force was measured in the steel plate, and the vertical displacement is the relative movement between the steel plate and the GFRP plate. As expected due to the extra flexibility of the experimental test setup, the numerical model is stiffer than the experimental one, this is a common problem when comparing numerical vs experimental structural responses [65]. The magnitude of the stiffness in the numerical model, was dependent on the adopted final geometry and support conditions, therefore due to its unknown variability, it is not expect to reach the same value as the one obtained in the experimental campaign. For the 15mm cover, there is a clear overestimation of the maximum reaction for both reduced and full integration, which is associated to the tensile matrix resistance and longitudinal 1-2 shear resistance being overestimated. Also, the adopted value of the fracture energy was estimated not measured in an experimental campaign. But for the 70mm cover, the maximum reaction is nearer the average experimental one, since the bearing is the collapse mode, and this is associated with the compressive resistance which was not estimated. It is also observed that for the 15mm cover there is no clear difference between adopting a residual stress of 15% or 80%, since the collapse mode is shear-out. However, for the 70mm cover clearly the 80% residual compressive stress produce better results when compared with the post peak values of the experimental campaign.

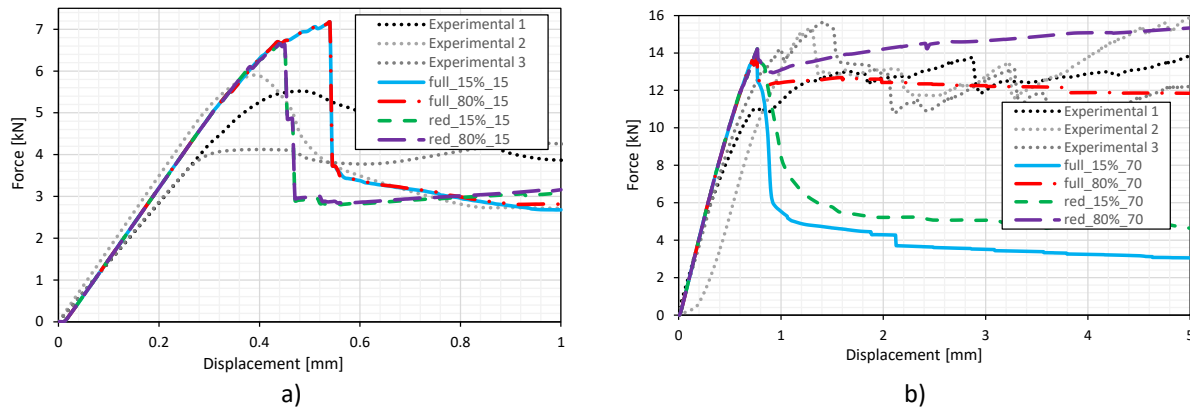


Figure 17 – Final matrix damage field distribution for a) implicit, b) explicit and c) ITE for the double lap test.

It is portrayed in Figure 18, the final shear 1-2 damage field for all numerical models with reduce and full integration, in which it is possible to perceive that for the 15mm cover it is clearly a full shear-out collapse, but for the 70mm cover there is a bearing collapse followed by a partial shear-out mode that does not finalize. This is according to what was observed in the experimental campaign until a relative displacement 5mm.

Also, only for the 70mm cover it can be seen in Figure 18, some difference in the final shear damage field distribution for 15% and 80% residual compressive stress. There is also some difference in the final

shear damage field distribution for reduce and full integration with 80% residual compressive stresses, just like the structural response in Figure 17 b).

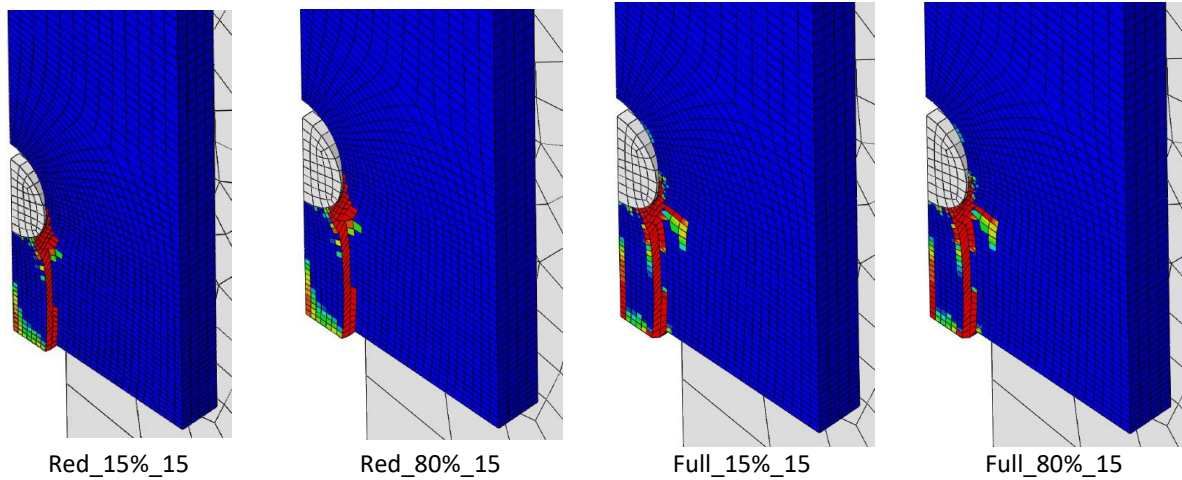


Figure 18 – Final shear damage distribution for 15mm of cover.

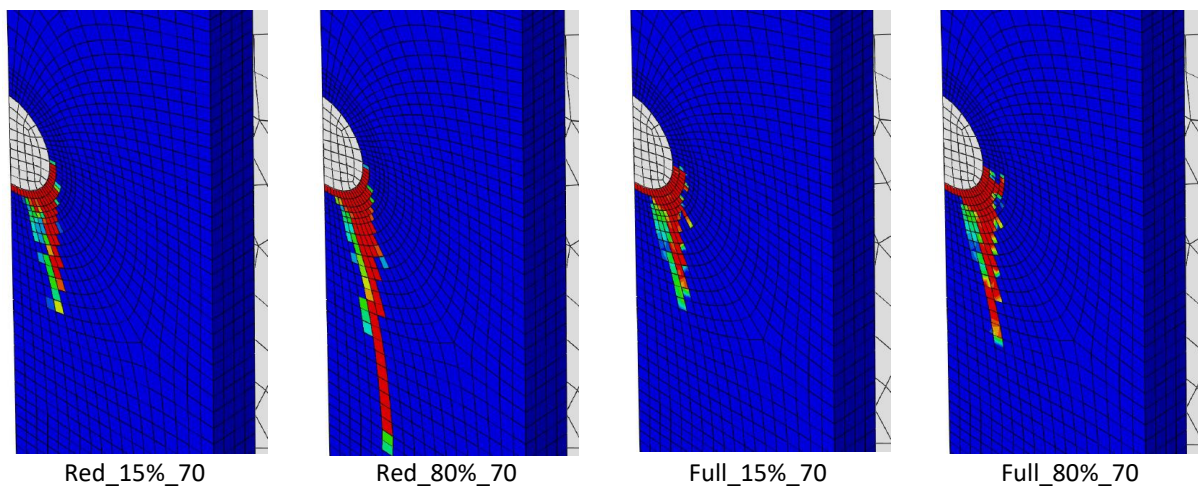


Figure 19 – Final shear damage distribution for 70mm of cover.

In Figure 20 a) it is presented the shear stress and shear damage evolution in the Gauss point nearest the circular opening perimeter at 30°C of the symmetry axis, in the GFRP plate. The results are presented for both 15mm and 70mm cover, with 15% and 80% residual compressive stress. These results are important, since they demonstrate that the adoption of a higher residual compressive stress has almost no influence for the residual shear stress, and this is more associated with the level of cover which influences indirectly the stress field. This is also the case for shear damage evolution displayed in Figure 20 b).

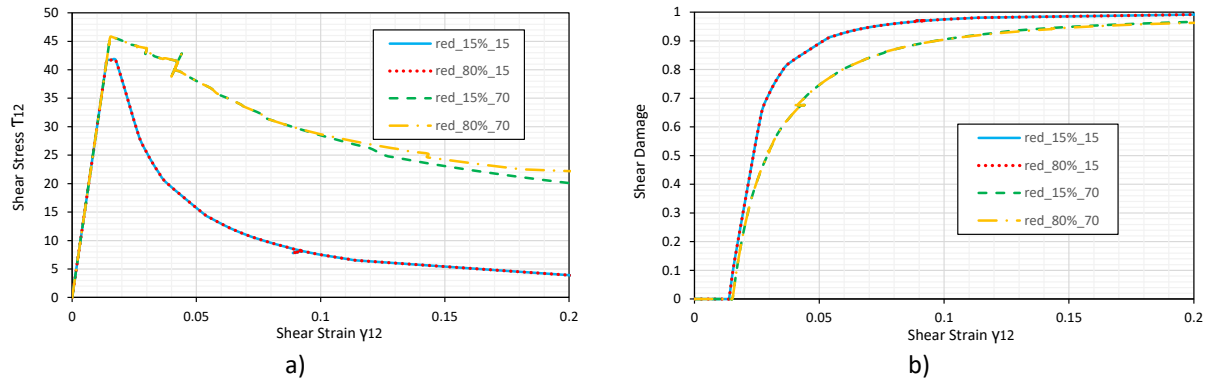


Figure 20 – Final matrix damage field distribution for a) implicit, b) explicit and c) ITE for the double lap test.

Finally to better understand that the proposed ITE algorithm does not overestimates the viscous energy and consequently the viscous damage, it is exhibited in Figure 21 the elastic damaged energy (ESE) and the viscous dissipation energy (VSE). As expected for the red_15%_15 there is a big reduction of force after 0.4s Figure 17, and as expected in this case, both the value of ESE and VSE increase, but after a given time step VSE stabilizes and ESE increases, demonstrating that the VSE is not dominating the structural response. For red_80%_70 this does not happen, this is due to the small force reduction during the structural response, in which VSE is always very small.

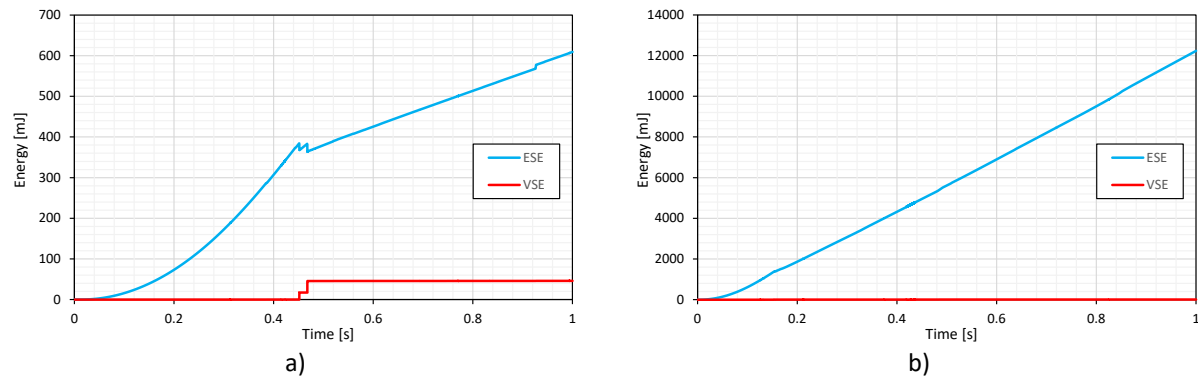


Figure 21 – Total elastic and viscous damage energy for a) reduce integration for 15mm cover with 15% residual compressive stress; b) reduce integration for 70mm cover with 80% residual compressive stress.

7 Conclusions

The main focus of this study is presenting a new 3D Hashin based damage model with residual stresses, and the proposal of an implicit to explicit (ITE) material time integration algorithm to be used in this and future damage models. This study was applied to published experimental campaign with specimens and beams made of GFRP composites.

- 1) The damage model was able to correctly estimate the structural response of CT and 3 Point bending tests, which are useful to correctly simulate the post peak response in materials exhibiting softening behaviour.

- 2) The possibility of using residual stress in the orthotropic Hashin based damage model, it was possible to correctly simulate the bearing collapse in GFRP connections. But the effect of residual stresses in the compressive behaviour has a small influence on the residual shear stress.
- 3) The use of ITE algorithm was robust, and in initial tests, present the same accuracy than a fully implicit material time integration method, when using the secant method in ABASQUS standard predictor-corrector algorithm.

7.1 Further Developments

In future research, it is expected to developed the orthotropic damage model, based in Hashin failure criterion, using residual shear stresses, that are important to simulate shear out collapse in composite connections. In addition, residual shear stress is also important for the correct numerical behaviour of 3D beam-to-column connection for cycle loads and dynamic analysis [57]. Also a variation of the 2D Tsai-Wu based damage model [61] is proposed for a 3D analysis, using the similar criterion used in this work. It is expected to use these orthotropic damage models in future design of GFRP structures.

8 References

- [1] El Kadi, M., Van Hemelrijck, D. and Tysmans, T. "Improving the Anchorage in Textile Reinforced Cement Composites by 3D Spacer Connections: Experimental Study of Flexural and Cracking Behaviors". *Journal of Composites Science* 6(12): 357 (2022).
- [2] Li, B., Gong, Y., Xiao, H., Gao, Y. and Liang, E. "A Two-Dimensional Model for Pin-Load Distribution and Failure Analysis of Composite Bolted Joints". *Materials* 14(13): 3646 (2021).
- [3] Martins, D., Proença, M., Correia, J. R., Gonilha, J., Arruda, M. and Silvestre, N. "Development of a novel beam-to-column connection system for pultruded GFRP tubular profiles". *Composite Structures* 171: 263-276 (2017).
- [4] Hu, H., Wei, Q., Liu, B., Liu, Y., Hu, N., Ma, Q. and Wang, C. "Progressive Damage Behaviour Analysis and Comparison with 2D/3D Hashin Failure Models on Carbon Fibre–Reinforced Aluminium Laminates". *Polymers* 14(14): 2946 (2022).
- [5] Kong, S. Y., Wong, L. S., Paul, S. C. and Miah, M. J. "Shear Response of Glass Fibre Reinforced Polymer (GFRP) Built-Up Hollow and Lightweight Concrete Filled Beams: An Experimental and Numerical Study". *Polymers* 12(10): 2270 (2020).
- [6] Girão Coelho, A. M., Toby Mottram, J. and Harries, K. A. "Finite element guidelines for simulation of fibre-tension dominated failures in composite materials validated by case studies". *Composite Structures* 126: 299-313 (2015).
- [7] Correia, J. R., Martins, D., Gonilha, J., Arruda, M., Andre, C., Nascimento, J. and Branco, F. "Clickhouse project an all composite emergency housing system". *CACM2015*(2015).
- [8] Arruda, M. R. T. and Lopes, B. "Pre-design guidelines for GFRP composite sandwich panels". *Engineering Solid Mechanics* 8(2): 169-186 (2020).
- [9] Arteiro, A., Catalanotti, G., Reinoso, J., Linde, P. and Camanho, P. P. "Simulation of the Mechanical Response of Thin-Ply Composites: From Computational Micro-Mechanics to Structural Analysis". *Archives of Computational Methods in Engineering* 26(5): 1445-1487 (2019).
- [10] Chowdhury, U. and Wu, X.-F. "Cohesive Zone Modeling of the Elastoplastic and Failure Behavior of Polymer Nanoclay Composites". *Journal of Composites Science* 5(5): 131 (2021).
- [11] Matzenmiller, A., Lubliner, J. and Taylor, R. L. "A constitutive model for anisotropic damage in fiber-composites". *Mechanics of Materials* 20(2): 125-152 (1995).

- [12] Lopes, B., Arruda, M. R. T., Almeida-Fernandes, L., Castro, L., Silvestre, N. and Correia, J. R. "Assessment of mesh dependency in the numerical simulation of compact tension tests for orthotropic materials". *Composites Part C: Open Access* 1: 100006 (2020).
- [13] ABAQUS "Abaqus Unified FEA-3DEXPERIENCE R2018". Systèmes, D. Rhode Island, 3DS-SIMULIA(2018).
- [14] ANSYS "ANSYS Structural Mechancis". Pennsylvania, ANSYS Inc.(2015).
- [15] Lapczyk, I. and Hurtado, J. A. "Progressive damage modeling in fiber-reinforced materials". *Composites Part A: Applied Science and Manufacturing* 38(11): 2333-2341 (2007).
- [16] Kang, I.-K. and Kim, S.-H. "Compressive Strength Testing of Hybrid Concrete-Filled Fiber-Reinforced Plastic Tubes Confined by Filament Winding". *Applied Sciences* 11(7): 2900 (2021).
- [17] Arruda, M. R. T., Castro, L. M. S., Ferreira, A. J. M., Martins, D. and Correia, J. R. "Physically non-linear analysis of beam models using Carrera Unified Formulation". *Composite Structures* 195: 60-73 (2018).
- [18] Nahas, M. "SURVEY OF FAILURE AND POST-FAILURE THEORIES OF LAMINATED FIBER-REINFORCED COMPOSITES". *Journal of Composites Technology and Research* 8: 138-153 (1986).
- [19] Kaddour, A. and Hinton, M. "Maturity of 3D failure criteria for fibre-reinforced composites: Comparison between theories and experiments: Part B of WWFE-II". *Journal of Composite Materials* 47(6-7): 925-966 (2013).
- [20] Hashin, Z. "Fatigue Failure Criteria for Unidirectional Fiber Composites". *Journal of Applied Mechanics* 48(4): 846-852 (1981).
- [21] Camanho, P. P. and Matthews, F. L. "A Progressive Damage Model for Mechanically Fastened Joints in Composite Laminates". *Journal of Composite Materials* 33(24): 2248-2280 (1999).
- [22] Hühne, C., Zerbst, A. K., Kuhlmann, G., Steenbock, C. and Rolfes, R. "Progressive damage analysis of composite bolted joints with liquid shim layers using constant and continuous degradation models". *Composite Structures* 92(2): 189-200 (2010).
- [23] Cheng, X., Wang, S., Zhang, J., Huang, W., Cheng, Y. and Zhang, J. "Effect of damage on failure mode of multi-bolt composite joints using failure envelope method". *Composite Structures* 160: 8-15 (2017).
- [24] Naderi, M. and Khonsari, M. M. "Stochastic analysis of inter- and intra-laminar damage in notched PEEK laminates". *Express Polymer Letters* 7: 383-395 (2013).
- [25] Linde, P., Pleitner, J., Boer, H. and Carmone, C. "Modelling and Simulation of Fibre Metal Laminates". 2004 ABAQUS Users' Conference, Boston Massachusetts, (2004).
- [26] Liu, Y., Zwingmann, B. and Schlaich, M. "Nonlinear Progressive Damage Analysis of Notched or Bolted Fibre-Reinforced Polymer (FRP) Laminates Based on a Three-Dimensional Strain Failure Criterion". *Polymers* 6(4): 949 (2014).
- [27] Wang, Y., Tong, M. and Zhu, S. "Three Dimensional Continuum Damage Mechanics Model of Progressive Failure Analysis in Fibre-Reinforced Composite Laminates". Structures, Structural Dynamics, and Materials Conference, California(2009).
- [28] Gutkin, R. and Pinho, S. T. "PRACTICAL APPLICATION OF FAILURE MODELS TO PREDICT THE RESPONSE OF COMPOSITE STRUCTURES". 18TH INTERNATIONAL CONFERENCE ON COMPOSITE MATERIALS, Lisbon-Portugal, (2009).
- [29] Warren, K. C., Lopez-Anido, R. A., Vel, S. S. and Bayraktar, H. H. "Progressive failure analysis of three-dimensional woven carbon composites in single-bolt, double-shear bearing". *Composites Part B: Engineering* 84: 266-276 (2016).
- [30] Olmedo, Á. and Santiuste, C. "On the prediction of bolted single-lap composite joints". *Composite Structures* 94(6): 2110-2117 (2012).
- [31] Mandal, B. and Chakrabarti, A. "Simulating Progressive Damage of Notched Composite Laminates with Various Lamination Schemes". *International Journal of Applied Mechanics and Engineering* 22(2): 333-347 (2017).

- [32] Wang, G.-D. and Melly, S. K. "*Three-dimensional finite element modeling of drilling CFRP composites using Abaqus/CAE: a review*".The International Journal of Advanced Manufacturing Technology 94(1): 599-614 (2018).
- [33] Liu, H., Liu, J., Ding, Y., Zhou, J., Kong, X., Harper, L. T., Blackman, B. R. K., Falzon, B. G. and Dear, J. P. "*Modelling damage in fibre-reinforced thermoplastic composite laminates subjected to three-point bend loading*".Composite Structures 236: 111889 (2020).
- [34] Camanho, P. P., Arteiro, A., Melro, A. R., Catalanotti, G. and Vogler, M. "*Three-dimensional invariant-based failure criteria for fibre-reinforced composites*".International Journal of Solids and Structures 55: 92-107 (2015).
- [35] Zhuang, F., Arteiro, A., Furtado, C., Chen, P. and Camanho, P. P. "*Mesoscale modelling of damage in single- and double-shear composite bolted joints*".Composite Structures 226: 111210 (2019).
- [36] Barbero, E. J. "*Finite Element Analysis of Composite Materials using ABAQUS*". London, CRC Press (2013).
- [37] Melro, A. R. "*Analytical and Numerical Modelling of Damage and Fracture of Advanced Composites*". Portugal, Phd, FEUP (2011).
- [38] Lemaitre, J. "*A Course on Damage Mechanics*". Verlag, Springer (1992).
- [39] Lemaitre, J., Benallal, A., Billardon, R. and Marquis, D. "*Thermodynamics and phenomenology*".In Continuum Thermomechanics - The Art and Science of Modelling Material Behaviour, Solid Mechanics and Its Applications 76: 209-223 Springer Netherlands (2002).
- [40] Wang, C., Roy, A., Silberschmidt, V. V. and Chen, Z. "*Modelling of Damage Evolution in Braided Composites: Recent Developments*".Mechanics of Advanced Materials and Modern Processes 3(1): 15 (2017).
- [41] Barbero, E. J. and Cosso, F. A. "*Determination of material parameters for discrete damage mechanics analysis of carbon-epoxy laminates*".Composites Part B: Engineering 56: 638-646 (2014).
- [42] Barbero, E. J., Cosso, F. A., Roman, R. and Weadon, T. L. "*Determination of material parameters for Abaqus progressive damage analysis of E-glass epoxy laminates*".Composites Part B: Engineering 46(Supplement C): 211-220 (2013).
- [43] Hashin, Z. "*Failure Criteria for Unidirectional Fiber Composites*".Journal of Applied Mechanics 47(2): 329-334 (1980).
- [44] Mulhern, J. F., Rogers, T. G., Spencer, A. J. M. and Hill, R. "*A continuum model for fibre-reinforced plastic materials*".Proceedings of the Royal Society of London. Series A. Mathematical and Physical Sciences 301(1467): 473-492 (1967).
- [45] Rosen, B. W. "*Mechanics of composite strengthening*"(1965).
- [46] Camanho, P. P. and Davila, C. G. "*Mixed-Mode Decohesion Finite Elements for the Simulation of Delamination in Composite Materials*".NASA/TM 211737: 1-37 (2002).
- [47] Rahimian Koloor, S. S., Karimzadeh, A., Yidris, N., Petrú, M., Ayatollahi, M. R. and Tamin, M. N. "*An Energy-Based Concept for Yielding of Multidirectional FRP Composite Structures Using a Mesoscale Lamina Damage Model*".Polymers 12(1): 157 (2020).
- [48] Lemaitre, J. and Desmorat, R. "*Engineering Damage Mechanics*". Berlin Heidelberg, Springer (2005).
- [49] Bazant, Z. P. and Oh, B. H. "*Crack band theory for fracture of concrete*".Materials and Structures 16: 155-177 (1983).
- [50] Oliver, J. "*A consistent characteristic length for smeared cracking models*".International Journal for Numerical Methods in Engineering 28: 461-474 (1989).
- [51] Forero, J. A., Bravo, M., Pacheco, J., de Brito, J. and Evangelista, L. "*Fracture Behaviour of Concrete with Reactive Magnesium Oxide as Alternative Binder*".Applied Sciences 11(7): 2891 (2021).
- [52] Borst, R., Crisfield, M. A., Remmers, J. J. C. and Verhoosel, C. V. "*Nonlinear Finite Element Analysis of Solids and Structures*". UK, Wiley (2012).
- [53] Duvaut, G. and Lions, J. L. "*Les Inéquations en Mécanique et en Physique*". Paris, Dunod (1972).

- [54] Geers, M. G. D., Brekelmans, W. A. M. and de Borst, R. "*Viscous Regularization of Strain-Localisation for Damaging Materials*", Dordrecht, Springer Netherlands (1994).
- [55] Dunne, F. and Petrinic, N. "*Introduction to Computational Plasticity*". New York, 1, Oxford University Press (2005).
- [56] Chaboche, J. L., Feyel, F. and Monerie, Y. "*Interface debonding models; a viscous regularization with a limited rate dependency*". International Journal of Solids and Structures 38: 3127-3160 (2001).
- [57] Martins, D., Gonilha, J., Correia, J. R. and Silvestre, N. "*Exterior beam-to-column bolted connections between GFRP I-shaped pultruded profiles using stainless steel cleats. Part 1: Experimental study*". Thin-Walled Structures 163: 107719 (2021).
- [58] Almeida-Fernandes, L., Silvestre, N., Correia, J. R. and Arruda, M. R. T. "*Fracture toughness-based models for damage simulation of pultruded GFRP materials*". Composites Part B: Engineering 186: 107818 (2020).
- [59] Liu, W., Feng, P. and Huang, J. "*Bilinear softening model and double K fracture criterion for quasi-brittle fracture of pultruded FRP composites*". Composite Structures 160: 1119-1125 (2017).
- [60] Almeida-Fernandes, L., Silvestre, N., Correia, J. R. and Arruda, M. "*Compressive transverse fracture behaviour of pultruded GFRP materials: Experimental study and numerical calibration*". Composite Structures 247: 112453 (2020).
- [61] Arruda, M. R. T., Almeida-Fernandes, L., Castro, L. and Correia, J. R. "*Tsai-Wu based orthotropic damage model*". Composites Part C: Open Access 4: 100122 (2021).
- [62] Chell, G. G. and Worthington, P. J. "*The determination of fracture toughness of a tough steel from invalid compact tension specimens of varying width and thickness*". Materials Science and Engineering 26(1): 95-103 (1976).
- [63] Xiong, Z., Zhao, C., Meng, Y. and Li, W. "*A damage model based on Tsai-Wu criterion and size effect investigation of pultruded GFRP*". Mechanics of Advanced Materials and Structures: 1-15 (2022).
- [64] CNR-DT-205/2007. "*Guide for the Design and Construction of Structures made of FRP Pultruded Elements*", Italy, Advisory Committee on Technical Recommendations for Construction (2008).
- [65] Martinavičius, D., Augonis, M. and Rui Tiago Arruda, M. "*Experimental and Analytical Study on Local Buckling Behavior of the Concrete-filled Thin-walled Welded Steel Columns*". Periodica Polytechnica Civil Engineering 64(3): 917-927 (2020).